EFFECT OF FOREBODY FORM ON THE AERODYNAMIC CHARACTERISTICS AND AIRFLOW AROUND AN AIRCRAFT MODEL UP TO HIGH ANGLES OF INCIDENCE

V Pesetsky, S Kalashnikov,
Central Aerohydrodynamic Institute, Zhukovsky, Russia
and D A Lovell
Defence Research Agency, Farnborough, United Kingdom

Abstract

Results of an investigation in the TsAGI subsonic wind tunnel T-103 with an aircraft model having five interchangeable forebodies are reported. The model was tested with and without wing leading-edge root extensions, with and without horizontal and vertical tail surfaces, for a range of angle of incidence from -4° to +50° and range of sideslip angles from -15° to +15°. Measurements of 6 force and moment components, flow visualization by mini tufts, smoke and oil are described. Pressure distributions have been measured at three cross sections on one of the forebodies. The effects of the forebody vortex flow on the aerodynamic characteristics have been analyzed.

Introduction

The cross section of the fuselage on an aircraft has historically been basically circular or elliptic, because the volume enclosed may thus be maximised and efficient structures may be defined for pressurised cabins on transport aircraft. While circular and elliptic sections generate benign flows at low angles of incidence the flow at the moderate and high angles of incidence required for highly manoeuvrable aircraft tends to become unpredictable. As a result aircraft stability and control can be compromised. The position of the onset of vortex flow and the type of vortex flow generated are dependent on small-scale features of the fuselage geometry, particularly in the tip region of the nose. Considerable research effort[1] has therefore been devoted to understanding and fixing this type of vortex flow. Nose suction[2], nose blowing[1],[3],[4],[5],[6] and mechanical devices[3],[7] have been investigated to provide flow control and predictable stability characteristics and, in some instances[2], to provide additional forces for aircraft control. A disadvantage of these systems is the potential interference they may cause with sensors mounted in the nose, particularly radar antenna.

An alternative approach[8] is to use a cross section shape for the nose that has very well defined flow characteristics at moderate to high angles of incidence. The chined nose, having a discontinuity in surface slope at the maximum fuselage width, produces a vortex flow that is insensitive to small-scale features of the nose shape. A potential disadvantage of this type of nose is that the existence of separated flow at relatively low angles of incidence may produce increased cruise drag and possibly an unacceptable flow environment for engine intakes on the fuselage. In addition, increasing vortex strength at higher angles of incidence could lead to an unacceptable non-linear rise in pitching moment that cannot be trimmed by the pitch motivators.

Previous computational work[9] has examined the effect of chine planform, depth and edge angle on the aerodynamic characteristics. The aim of the present work is to investigate experimentally the effect of changing the included angle of the chine edge, for a nose having a fixed shape in planform and elevation. Starting from an elliptic section (included angle 180°) 5 alternative nose cross sections have been investigated having progressively sharper edges, with nose 5 having a cusped cross section (included angle 0°).

The work has been completed at the Russian Central Aerohydrodynamic Institute (TsAGI) in Zhukovsky, under contract to the Defence Research Agency at Farnborough, UK.

Wind Tunnel

The experimental investigations were conducted in the TsAGI T-103 low speed wind tunnel which has a closed-circuit and an open test section. The return circuit of the T-103 wind tunnel is located in the vertical plane. The nozzle exit section is elliptic in cross section, with a horizontal axis of 4 m and a vertical axis of 2.33m. The length of the working section is 4m. The tunnel flow velocity can be smoothly regulated over the range 10 to 100m/s. Within a region with dimensions of 3.2m wide by 1.2m high and extending 1.5m downstream, in which the model was tested, the uniformity of dynamic pressure and flow angularity from the nozzle edge are characterized by the following values of maximum deviation from the mean values:

Dynamic pressure:	+1.0% to -1.0%
Flow angularity in vertical plane:	+0.2°
Flow angularity in horizontal plane:	+0.2°

The variation of static pressure along the test section

axis is insignificant (dC_p/dX=0.0008 per m). The flow turbulence in the empty wind tunnel is 0.4%.

Model Description

The aircraft model (fig 1 "ALISA") has a trapezoidal mid-mounted wing in a conventional aft-tail arrangement. The fuselage has five interchangeable forebodies with the range of cross-section shapes shown in figure 2. The planform and elevation of the forebodies is constant, with the chine-edge included angle varying from 180° (elliptic section) to 0° (cusped edge). The model lay-out is shown in figure 1 and the values of the geometric parameters for the model are given in table 1. The model has a removable strake for the wing and horizontal and vertical tail surfaces. The nose 4 has a total of 78 surface pressure tappings at three sections.

Table 1 Model Geometry

Wing	
Span	1.2649 m
Basic area	0.4 m^2
MAC	0.35417 m
Leading edge sweep	40°
Aspect ratio	4
Taper ratio	0.25
Profile thickness	5%
Strake leading edge sweep	72°
Fuselage	
Length	1.5 m
Span	0.177 m
Horizontal tail	
Relative area	0.3
Span	0.3099 m
Aspect ratio	1.6
Taper ratio	0.4
Leading edge sweep	40°
Vertical tail	
Relative area	0.149
Height	0.3 m
Aspect ratio	1.5
Taper ratio	0.336
Leading edge sweep	40°

Experimental Technique

The experimental investigations included measurements of overall force and moment components, flow visualization by mini tufts, smoke and colour oil film for 5 noses, as well as measurements of the pressure distribution at three cross sections on nose 4. The test programme is listed in table 2.

Force and moment tests

The model was tested using the T-103 six-component mechanical balance to which it was attached at three points by a strip support system. The two forward points which define the axis of model rotation for changing the angle of incidence are located 1.2 m. apart, and the third tail point is 0.75 m behind the rotation axis. The model was tested in an inverted position and the angle of incidence was measured relative to the fuselage centre line. The tests in the T-103 wind tunnel were performed at an airflow speed of 50 m/s and the test results were processed according to the standard methodology for the T-103 wind tunnel. The results were corrected for blockage effects, flow boundary effects, drag of the strip suspension system, and moments from the strip suspension system. The aerodynamic coefficients C_D, C_L, C_m have been calculated in wind-axes coordinate system and the coefficients C_y, C_l, C_n in body-axes coordinate system. The force coefficients are non-dimensionalised using the free-stream dynamic

Table 2 Test Programme

TEST	NOSE	STRAKE	HT, ι^o	VT	α^o	β^o	Comment
F&M	1	off	on	on	15, 25	0, 15	kaolin
F&M	1	off	on	on	15, 25	-15 to +15	with strip
F&M	1 to 5	on, off	on, off	on	-5 to +50	-15 to +15	nose 1 with strip.
F&M	4	on	on, off	off	-5 to +50	-15 to +15	
F&M	4	on, off	on +15 to -30	on	0, 10	0	
Tuft on wing, strake, fuselage	1 to 5	on, off	on	on	0, 10, 20, 30, 40, 50	0, 10	
Oil film	1, 4	on, off	on	on	10, 20, 40	0, 10	
Smoke wire	1 to 5	on, off	on	on	10, 20, 40	0, 10	
$TiCl_4$	1 to 5	on, off	on	on	10, 20, 40	0, 10	
Pressure distribution	4	on, off	on	on	0, 10	0, 5, 10, 15	

pressure and the wing area. In computing the C_m coefficients the wing mean aerodynamic chord was used as the additional characteristic length. The lateral moments C_l and C_n are referred to the same area and the wing span. The moment coefficients have been calculated relative to a moments centre on the fuselage centre line 0.851m from the model nose. The connection points between the suspension system and the balance had the following coordinates relative to the leading edge of the reference wing section:

X_o = 0.7565 m Y_o = -0.0554 m

The accuracy of measurement of the aerodynamic coefficients, determined from a statistical analysis of ten runs, was:

$RMSC_D$ = 0.0003 $RMSC_L$ = 0.002
$RMSC_m$ = 0.0003 $RMS(C_L/C_D)$ = 0.5

Oil film and kaolin techniques

To investigate the boundary-layer condition and the flow on the model surface a "liquid kaolin" method and a colour oil film method were used. The "liquid kaolin" method is used to visualise the zones of laminar and turbulent flow in the boundary layer on the model. The "liquid kaolin" comprises a suspension of kaolin powder (white clay) in ether. This suspension is applied to the painted model surface. The ether vaporizes rapidly in regions of turbulent flow, leaving a thin kaolin layer of white colour, whereas in regions of laminar flow the ether does not evaporate and the surface remains black. The border between black and white zones on a model surface indicates the line of boundary layer transition which is photographed after the run. This technique was used to determine the areas of laminar and turbulent flow on the elliptical nose.

For visualization of the flow pattern on the upper model surface by means of colour oil film the model is installed on the T-103 sting rig (VV-2) to provide a good view of the model surface from both the side and from above. Elements of the model were painted with an oil film made up of different colours. Under the action of dynamic pressure the oil paint spreads over the model surface, resulting in visualization by different colours of the flow streamlines so that the influence of regions of the flow may be separated. The time for establishment of a flow pattern on the model surface was typically several minutes. The flow pattern was recorded by means of a video recorder during the run and photographed from various angles by a still camera after the run. Oil film visualisation studies were done for nose 1 and nose 4 (e.g. fig 4). Air flow speed for these investigations was 50m/s.

Mini-tufts flow visualisation

To visualise the flow on the model surface mini tufts method were used. Thin tufts 15mm long, diameter 0.1mm were pasted on the model surface which was illuminated by short light pulses, which caused luminescence. The flow pattern was recorded simultaneously by a still camera and by a video recorder.

The pulsing illuminator was placed above the model in the test section outside the airflow. Photo and video cameras were positioned to receive the best reflected light from the tufts on the model surface. The time interval between light pulses was approximately 3 sec. A time interval of 1 sec between the light pulses was used for the video recording. The tests were conducted at a flow speed of 50m/s.

Smoke flow visualization

Vortices formed on the forebodies and on the strake were visualized by using a heated wire coated with glycerine to generate smoke, and by using $TiCl_4$ vapour. The smoke wire method was used for visualising the flows around the vortices, while the $TiCl_4$ method enabled the vortex core positions to be observed. For these visualization tests the model was installed on a three-point rigid platform.

The arrangement of the smoke wire on the noses and strake is shown in fig. 3. The wire was mounted on insulated supports at a height of 4mm above the lower surface of the model. The actual distance of the wire from the surface of the model varied between 2 and 4mm. In the present experiments Wolfram wire with a diameter of 0.1mm and length of 0.6m was used. The forward end was fastened to an earthing rack at the nose part of model, and the rear end to an insulated plug on the wire system. To create a smoke filament the wire was coated with glycerin before each run. Under the action of surface tension forces glycerin drops having a diameter 0.2 - 0.3mm were formed. When heated by an electrical current the boiling glycerin drops create smoke filaments that are swept into the main flow.

The vapour from $TiCl_4$ was injected into the area of vortex formation through drain holes in the nose of the model, as shown in fig. 3. The reservoir tank for the $TiCl_4$ was placed inside the model. The $TiCl_4$ vapours were ejected from the tank by low-pressure nitrogen (< 10 Pa).

Pictures of the vortex structures were taken from two directions - from the side and from above. The systems for generation of smoke were mounted only on one side of the model and the effects on the two sides of the nose were examined by recording the flow visualisation for positive and negative values of sideslip angle. The synchronisation of the

visualization processes and the photography was electronically controlled. The mini tufts were left on the surface of the model during the smoke visualisation investigations. The flow velocity for these investigations was 20m/s.

Pressure measurement

For the measurements of surface pressure the model was mounted on the T-103 sting rig (VV-2) which permitted angles of incidence of the model from -3° to 50°, relative to the reference plane of the fuselage. The tests were conducted at flow velocity of 50 m/sec. Pressures were measured at 78 points on the surface of the model using KP-48 scanivalves, equipped with PD-4 pressure gauges, covering the range -1500 to +1500 Pa with an error between 0.1 and 0.3%. The results of tests are presented as pressure coefficients ($C_p=p-p_\infty/q$, where p is the static pressure on the model surface, p_∞ is the free-stream pressure and q is the dynamic pressure). A correction was applied for the variation of q across the wind tunnel section. The angles of incidence for which pressures were measured have not been corrected for the effect of the flow boundaries. The correction in degrees to the angle of incidence due to this effect is given by:

$$\alpha = \alpha_{geom} - 1.889*C_L$$

Test results

The position of transition from laminar to turbulent flow on the elliptical nose was determined using the kaolin technique, and a transition strip position on the nose was chosen. A wire of diameter 0.3mm was pasted on the undersurface starting about 30mm from nose and on line at an angle of 70° to the vertical plane of symmetry. All subsequent tests of the model with nose 1 were conducted with this strip. There was no need for a transition strip to fix the primary separation for noses 2 to 5 as these have a sharp edge.

Characteristics without wing LERX

Analysis of the results up to an angle of incidence of 10° shows that the aerodynamic characteristics of the model $C_L(\alpha)$, $C_y(\alpha)$, $C_m(\alpha)$, $C_l(\beta)$, $C_n(\beta)$ are linear (fig 5 to 8), and the flow over the model is only separated on the noses with sharp side edges and at the wing tips. This is confirmed by the results obtained with mini tufts and oil film. For zero sideslip angle on the elliptical nose there is insignificant flow of oil from the bottom surface to the top. There are no signs of traces from nose vortices. With a sideslip angle of -10° there is a change of direction of the streamlines on the model surface and a slight increase in the flow from the bottom surface to the top on the windward side of the nose and a slight decrease on the leeward side.

On the other noses the presence of sharp side edges leads to the formation of moderately intense vortices. Thus for sideslip angles 0° and -10° on noses 4 and 5 vortices lie in the cavity adjacent to the side edges. At a sideslip angle of -10° the vortex on the leeward side is weaker. The vortices formed on the noses with sharp edges can be seen very well on the photos of the smoke patterns. The vortices produce an increased level of suction on the upper surface of the nose and hence increased pitching moment on the model (fig 7).

The variation of lift and side forces, pitching, rolling and yawing moments with the angles of incidence and sideslip become nonlinear at angles of incidence greater than 10°. The onset of non-linearity is connected with the development of flow separation on all elements of the model (fig 5 to 9). The form of the cross section of the nose has a major influence on the aerodynamic characteristics of the model at these angles of incidence, particularly on lift and pitching moment.

The sharp nose side edges increase lift and pitching moment of model for $\alpha > 13^{\circ}$ (fig 5, 7). At angles of incidence in the range 13° to 15° on the complete model with noses 3, 4 and 5 there is a region of local instability in pitching moment (fig 7). More pronounced non-linearities in the dependencies of side force, rolling and yawing moments on sideslip angle begin at angles of incidence greater than 20°.

For an angle of incidence range of 10° to 20° analysis of the mini tuft and oil film patterns shows that the change of the nose form has a fundamental effect on the flow over the nose and the root section of the wing. The flow over the outer part of the wing and over the horizontal tail is practically independent of the nose shape.

At an angle of incidence 20°, unyawed, the flow separates at the wing leading edge and rolls up into a vortex. This vortex leaves the trailing-edge of the wing at approximately mid-span. Outboard of this vortex there is a wing leading-edge stall. The flow also separates from the leading edge of the horizontal tail and rolls up into a vortex. The trace of this vortex on the upper surface of the horizontal tail is very apparent in the mini-tuft and oil film patterns. At a sideslip angle of 10° and an angle of incidence of 20°, vortices on the leeward side of the wing and the horizontal tail are displaced towards the wing and tail tips, and those on the windward side are displaced to the root sections. The area of the leading edge stall is thus reduced on the leeward side of the wing and increased on the windward side.

The flow over the elliptical-section nose (1) at an angle of incidence of 20°, without sideslip, is characterized by the existence of a vortex system. There are two vortices originating from the tip of the fuselage nose, which are located near to the plane of symmetry, and two side vortices, formed on the side

surfaces of the nose. At a sideslip angle of 10^{o} the vortices on the windward side are displaced towards the plane of symmetry, and those on the leeward side to the lateral edge.

Moving from nose 1 to nose 2, a similar flow picture is observed qualitatively at an angle of incidence of 20^{o}. For zero sideslip and $\alpha=20^{o}$ a system of four vortices is visible on the nose. Again there are two vortices originating from the tip of the fuselage nose, which are located near to the plane of symmetry, and two side vortices formed on the side surfaces of the nose. The vortex intensities on nose 2 are greater than those from nose 1. At non-zero angles of sideslip there is a similar influence on vortex positions to that seen on nose 1.

The flow over the model at $\alpha=20^{o}$ for noses 3, 4 and 5 is qualitatively similar. On the flow visualisation photographs vortices are only visible springing from the sharp lateral edges of the noses. At non-zero angles of sideslip the vortices deviate towards the free stream direction as for noses 1 and 2. With a further increase in the angle of incidence the leading-edge stall spreads to cover the whole of the wing and horizontal tail surfaces. This results in a reduction of the lift- curve slope. The maximum lift coefficient is reached at an angle of incidence between 32^{o} and 33^{o}. For the model with the elliptical nose $C_{Lmax}=1.66$, whereas with noses 4 and 5 $C_{Lmax}=1.95$ (fig 5).

Over the range of angle of incidence 26^{o} to 28^{o} for the elliptical nose, and for $\alpha=28^{o}$ to 32^{o} for the other noses, the model loses stability in roll and yaw i.e. the moment derivatives $C_{l\beta}$ and $C_{n\beta}$ change sign.

By an angle of incidence of 30^{o} practically all of the upper wing surface is influenced by a leading edge stall for all of the nose variants. At this angle of incidence the nose vortices remain, being displaced upwards from the surface of the model. Flow separation covers the top surface of the wing and tail, and is present on the fuselage in the area of the wing trailing edge. At $\alpha = 50^{o}$ without sideslip, the nose vortices are higher above the model surface for all nose variants and burst over the part of the fuselage where the sections changes to elliptic. This is visible on the photographs of the smoke visualisation. For non-zero sideslip angles the position of vortex breakdown of the leeward vortex is displaced downstream, while that of the windward vortex is displaced upstream. By $\alpha=50^{o}$ the onset of flow separation on the fuselage has moved forward to the region of the wing leading edge. The mini-tuft flow pattern shows that the nose vortices on the top surface of the nose persist at high angles of incidence.

Characteristics of model with wing LERX

With the LERX installed on the wing the angle of incidence below which the nose form has little influence on the aerodynamic characteristics is increased to 15^{o}. The LERX produces an increase in lift and introduces nonlinearity in $C_{m}(\alpha)$ at small angles of incidence (fig 11). This is associated with the formation of a vortex on the sharp leading-edge of the strake at angle of incidence of about 4^{o}. The strake vortex can be seen in the smoke patterns, the surface oil films and the tuft patterns at an angle of incidence of 10^{o}. At $\alpha=10^{o}$ there is little change in the effect of the LERX on the nose flow as sideslip is increased from 0^{o} to -10^{o}.

As has been shown by smoke wire and oil film flow visualisation on noses 1 and 2, for the whole range of incidence investigated, vortices exist independently of the LERX vortices. For noses 3, 4 and 5 at angles of incidence greater than 10^{o} a single vortex is formed. This begins on the nose and passes over the wing LERX. With increase in the angle of incidence the vortices are displaced upwards and towards the model centre line, and their intensity is increased. The LERX vortex improves the flow over the inboard wing, thus restricting the movement inboard of the tip stall.

The analysis of the tuft and smoke flow patterns also shows that between $\alpha=20^{o}$ and 30^{o} at zero sideslip the LERX vortex breaks down in the region of the wing trailing edge. With further increase in the angle of incidence the point of vortex breakdown moves upstream. At $\alpha=40^{o}$ vortex breakdown occurs at the wing leading-edge junction with the strake for all nose variants. At non-zero angles of sideslip vortex breakdown is again displaced upstream on the windward side and downstream on the leeward side .

Pressure measurements on nose 4

The pressure distributions measured at three cross sections on nose 4 on the model without the LERX are shown in fig 14. At $\beta=0^{o}$ the flow is practically symmetric. With increase of incidence the suction peaks on the top surface under the vortex move towards the model centre line. Moving aft on the body from section I to section II and to section III there is a reduction in the magnitude of the suction peaks because the vortex moves away from the model surface. Above $\alpha=45^{o}$ at sections I and II the magnitude of the suction peaks reduces with increase of incidence. For section III maximum suction occurs in the range $\alpha=30^{o}$ to 35^{o}, which is again connected with the deviation of the vortex path from the model surface at high incidence.

At non-zero sideslip angles the vortex intensity differs on the two sides of the nose, as might be expected. For all the sideslip angles investigated the maximum suction on the windward side exceeds that on the leeward side, for angles of incidence below that for vortex breakdown. For the leeward side of

section I a uniform rate of growth of suction peak occurs as incidence is increased. The windward suction peaks behave in a similar way to that seen at zero sideslip; reaching a maximum at some incidence (fig 14). By section III suction peaks are absent on the leeward side, confirming the deviation of the vortex from the fuselage. Also, for section III at sideslip angles greater than 10^{o}, the maximum suction on the windward side reduces and the suction peak is displaced almost to the model centre line. It is possible to interpret this as the flow from the windward side moving to the leeward side.

For zero sideslip with the LERX fitted a symmetric flow picture is also obtained. As on the model without LERX, increase of incidence causes the suction peaks generated by the vortices to move nearer to the plane of model symmetry. Due to the presence of the LERX the change of shape from section II to section III is not accompanied by a reduction in the magnitude of the suction peaks. The peaks are located further outboard from the plane of model symmetry.

As noted for the model without LERX, at non-zero angles of sideslip with LERX the intensity of the vortices on the two sides of the fuselage differ, and the angle of incidence for the onset of vortex breakdown differ (fig 14). The reduction in the magnitude of suction peaks occurs at a lower angle of incidence. For section I the value of the suction peak on the leeward side is in general a little higher on the model with LERX. For the windward side of section III at $\beta=10^{o}$, 15^{o} and $\alpha=30^{o}$ to 50^{o}, and at $\beta=15^{o}$ at $\alpha=50^{o}$ for all sections, the upper surface pressure is approximately constant indicating that the flow has completely stalled. Comparing the pressures measured on the bottom fuselage surface at section III, the LERX causes an increased pressure at all sideslip angles.

Chine edge angle

The variation of increments in lift, drag, pitching moment and L/D with chine edge angle is shown on fig. 13. Here $\Delta C_{Lmax}=C_{Lmax\varphi}-C_{Lmax\varphi=90^{o}}$, $\Delta C_{Do}=C_{Do\varphi}-C_{Do\ \varphi=90^{o}}$, $\Delta(L/D)_{max}=(L/D)_{max\varphi}-(L/D)_{max\varphi=90^{o}}$ and $\Delta dC_m/dC_L = dC_m/dC_{L\varphi}-dC_m/dC_{L\varphi=90^{o}}$. ΔC_{Do} is a minimum and $\Delta(L/D)_{max}$ is a maximum for chine edge angle $\varphi=62^{o}$ for the model without LERX. The value of ΔC_{Do} is equal to -0.003 and value of $\Delta(L/D)_{max}$ is equal to 1.0. With the LERX fitted to the model there is only a small variation of ΔC_{Do} and $\Delta(L/D)_{max}$ with chine edge angle.

The chine edge angle has influence on the value of dC_m/dC_L above an angle of incidence of 10^{o}. Maxima of ΔC_{Lmax} and dC_m/dC_L occur for values of edge angle between 0^{o} and 15^{o}. The value of ΔC_{Lmax} is equal 0.3 for model without LERX and 0.16 for model with LERX.

Conclusions

(1) Comprehensive measurements of the aerodynamic characteristics and flow over the model have been made for five nose shapes in T-103 wind tunnel, for a range of angle of incidence $\alpha= -5^{o}$ to 50^{o}.

(2) The investigations have shown that the change of nose cross section from elliptical to complex with sharp edges produces increases in lift and pitching moment on the model for a range of moderate to high angles of incidence ($\alpha=15^{o}$ to 50^{o}).

(3) The aerodynamic characteristics of the model at high angles of incidence are determined by the position and intensity of the vortices formed on the nose.

(4) There is a minimum of C_{Do} and a maximum of $(L/D)_{max}$ for a chine edge angle $\varphi=62^{o}$ for the model without LERX and maximum of lift and dC_m/dC_L for a chine edge angle in the range 0^{o}-15^{o}.

References

1 Rao D M, Campbell J F; "Vortex flow management techniques." Progress in Aerospace Sciences Vol 24 pp173-224, 1987

2 Edwards G F, Ross A J, Jeffries E B, O'Leary C O; "Dynamic tests to demonstrate lateral control using forebody suction on large-scale models in the DRA 24ft wind tunnel." AGARD CP-548, FMP Symposium, Annapolis, October 1993

3 Malcolm G N, Ng T T, Lewis L C, Murri D G; "Development of non-conventional control methods for high angle of attack flight control using vortex manipulation." AGARD FDP Symposium, Madrid, October 1989

4 Cornelius C C, Pandit N, Osborn R F, Guyton R W; "Experimental study of pneumatic control of forebody vortices at high alpha.
" Journal of Aircraft Vol 31, No 1, Jan-Feb 1994

5 Agosta-Greenman R M, Gee K, Cummings R M, Schiff L B; "Computational investigation of tangential slot blowing on a generic chined forebody." Journal of Aircraft Vol 32, No 4, July-Aug 1995

6 Cummings R M, Schiff L B, Duino J D; "Experimental investigation of tangential slot blowing on a generic chined forebody." Journal of Aircraft Vol 32, No 4, July-Aug 1995

7 Rao D M, Murri D G; "Exploratory investigation of deflectable forebody strakes for high-angle-of-attack yaw control." AIAA-86-0333, 24th Aerospace sciences Meeting, Reno, 1986

8 Roos F W, Kegelman J T; "Aerodynamic characteristics of three generic forebodies at high angles of attack." AIAA-91-0275, 29th Aerospace Sciences Meeting, Reno, 1991

9 Ravi R, Mason W H; "Chine-shaped forebody effects on directional stability at high-a." Journal of Aircraft, Vol 31, No 3, May-June 1994

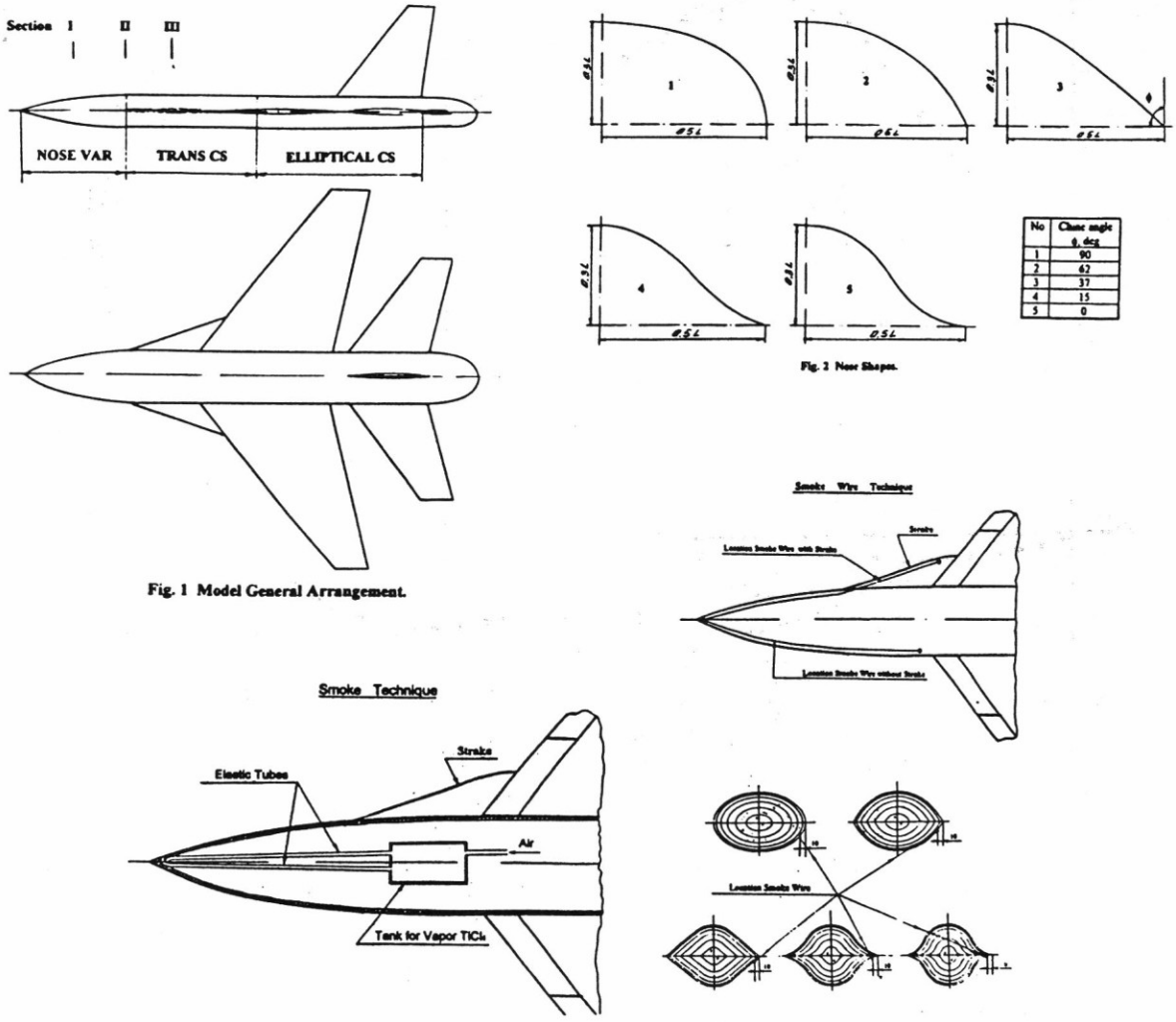

Fig. 1 Model General Arrangement.

Fig. 2 Nose Shapes.

Fig. 3 Smoke Technique.

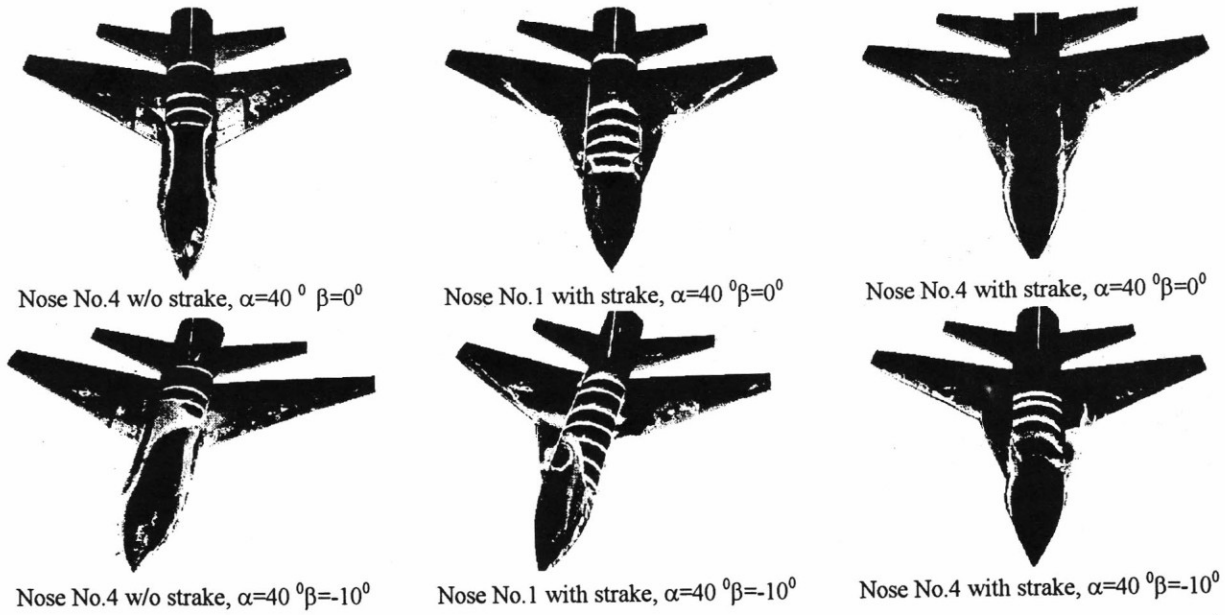

Nose No.4 w/o strake, $\alpha=40^0$ $\beta=0^0$ | Nose No.1 with strake, $\alpha=40^0\beta=0^0$ | Nose No.4 with strake, $\alpha=40^0\beta=0^0$

Nose No.4 w/o strake, $\alpha=40^0\beta=-10^0$ | Nose No.1 with strake, $\alpha=40^0\beta=-10^0$ | Nose No.4 with strake, $\alpha=40^0\beta=-10^0$

Fig. 4 Oil Flow

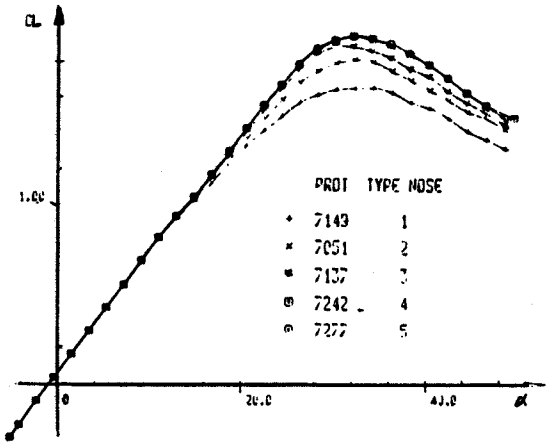

Fig. 5.

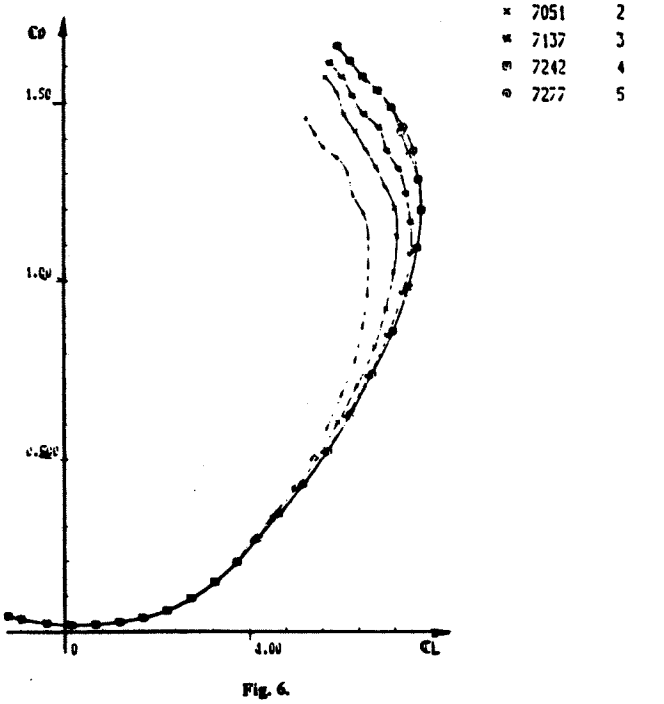

Fig. 6.

PROT TYPE NOSE
+ 7149 1
× 7051 2
7137 3
7242 4
7277 5

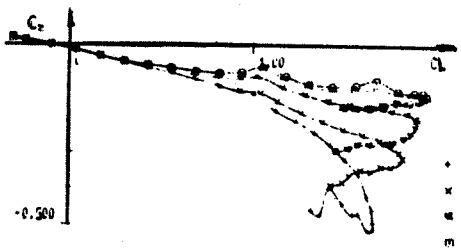

Fig. 7.

PROT TYPE NOSE
+ 7149 1
× 7051 2
7137 3
7242 4
7277 5

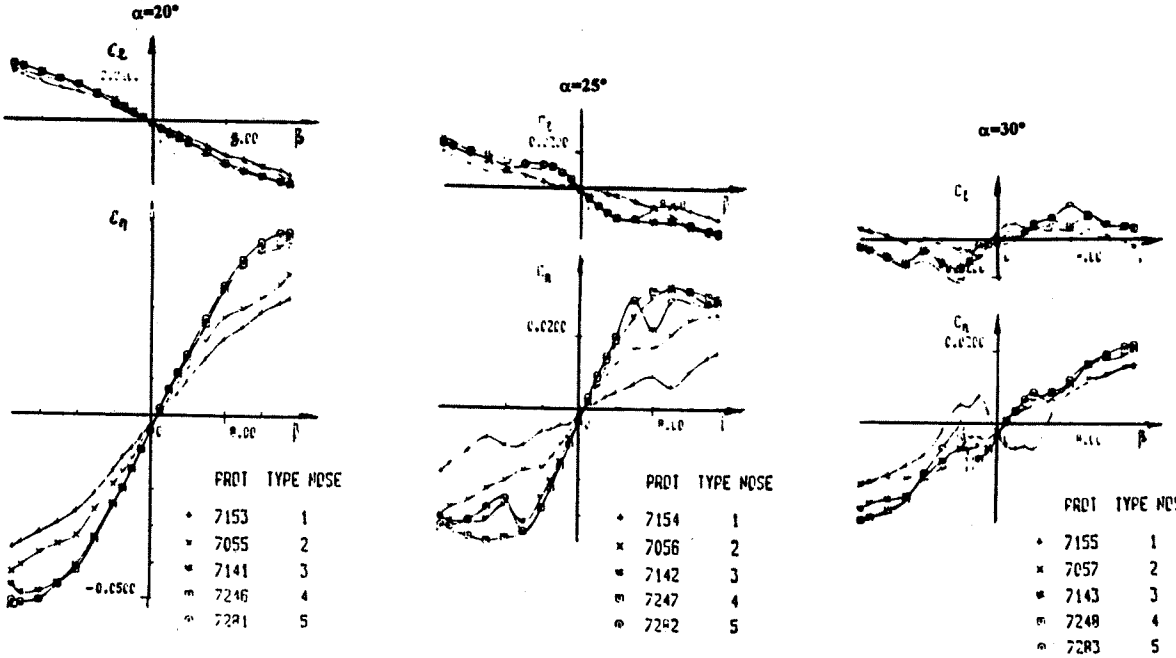

Fig. 8.

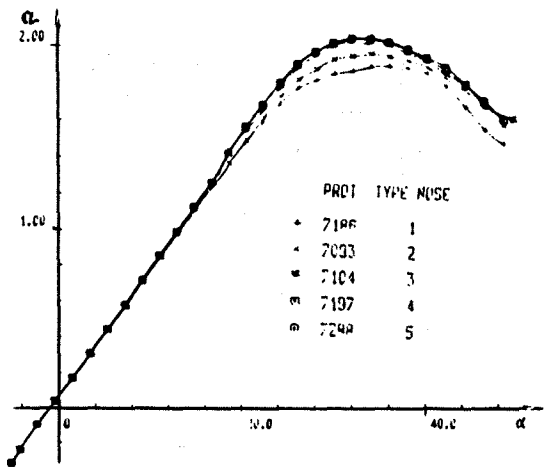

Fig. 9.

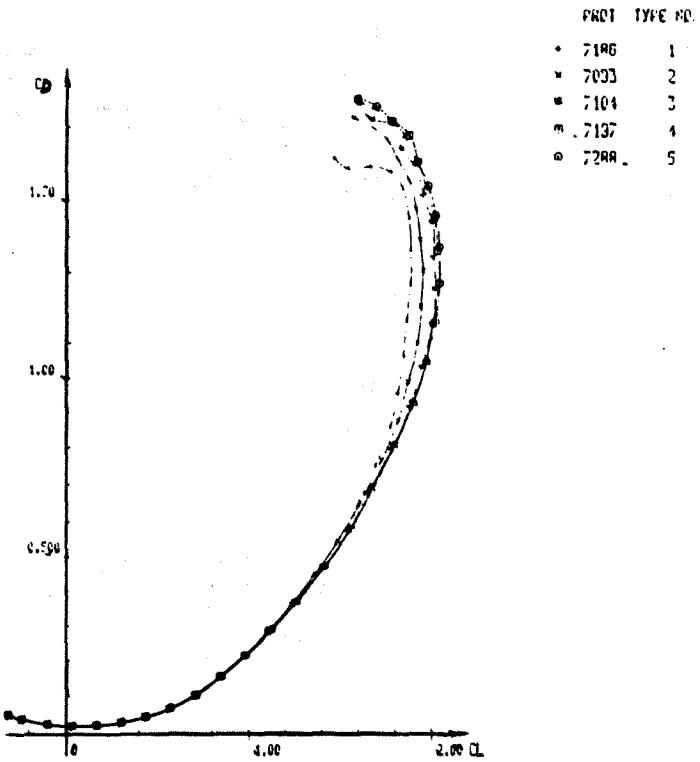

Fig. 10.

Fig. 11.

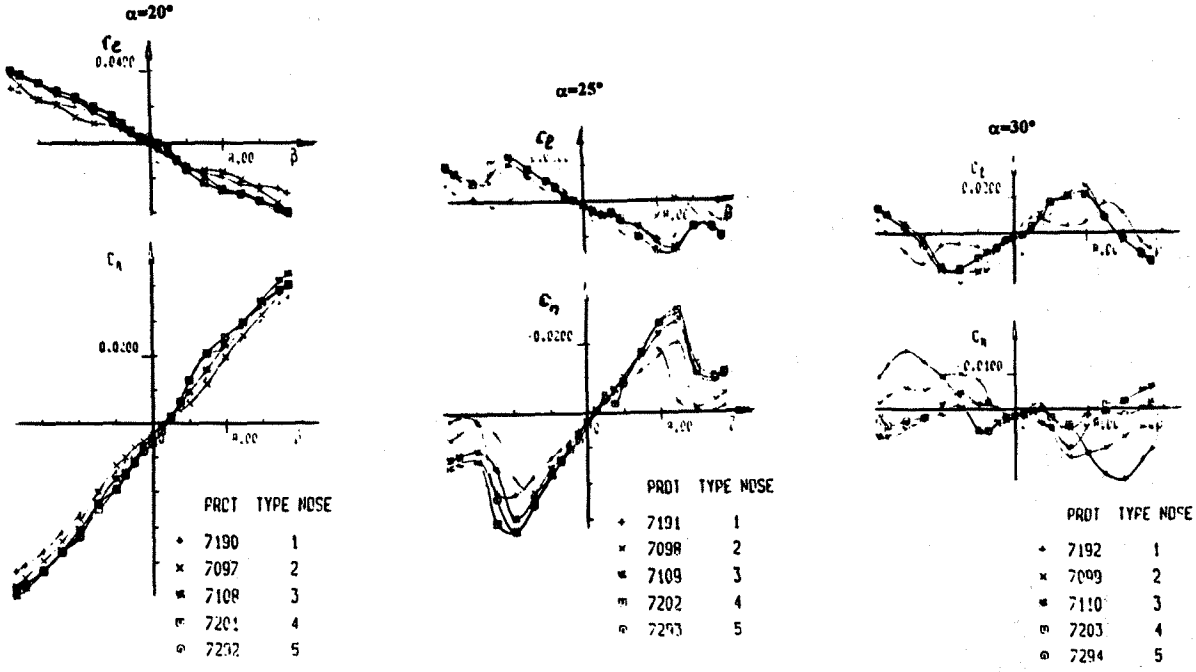

Fig. 12.

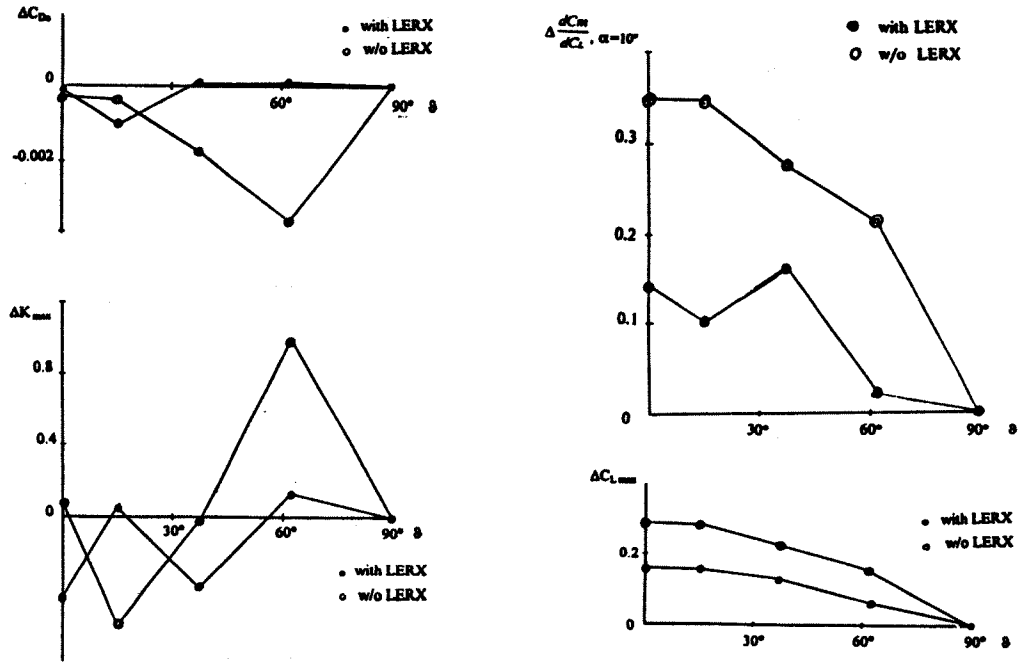

Fig. 13.

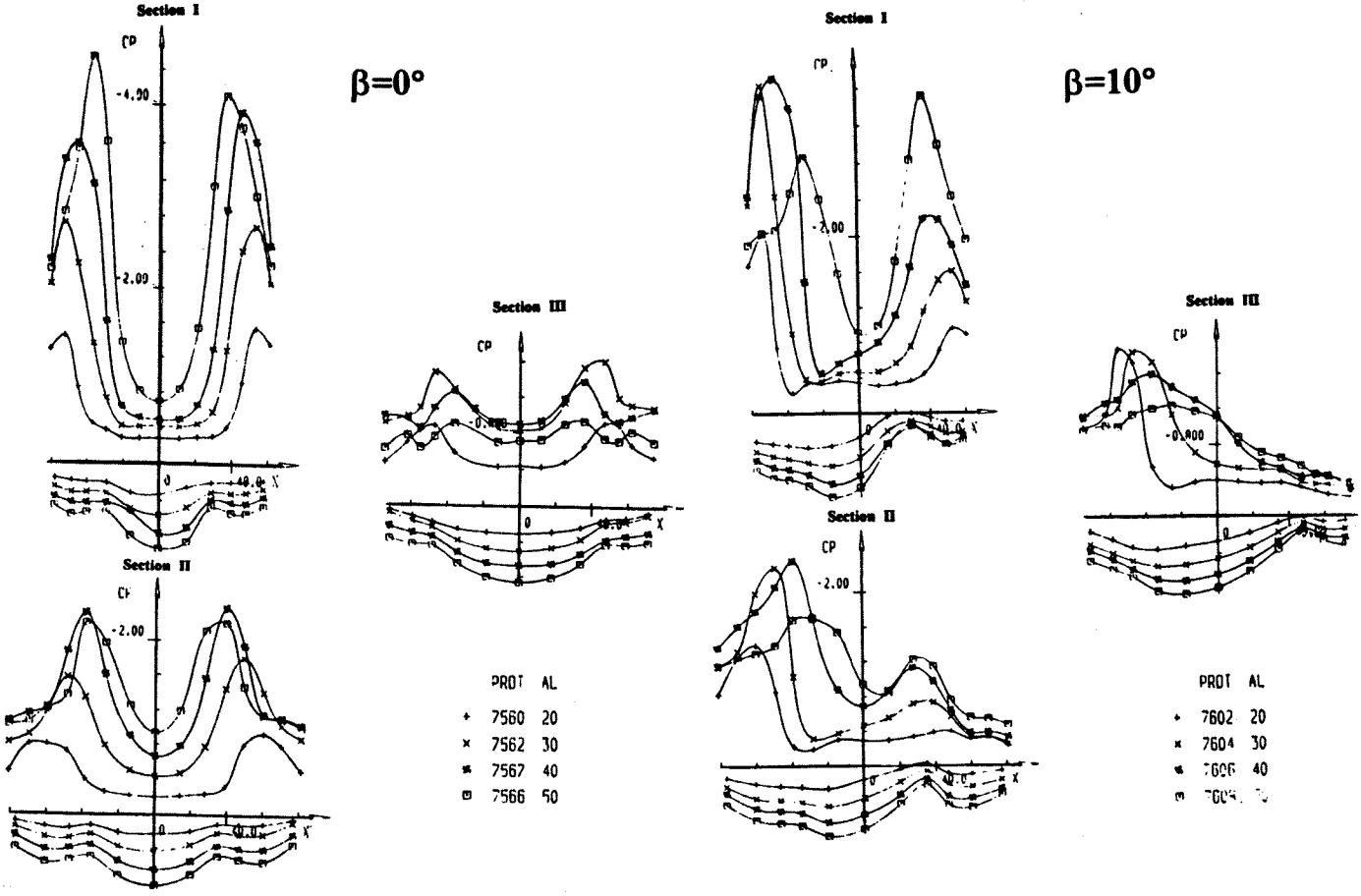

Fig. 14 Pressure Distributions for Nose 4.